

3D-Printed Cathodes of $\text{LiMn}_{1-x}\text{Fe}_x\text{PO}_4$ Nanocrystals Achieve Both Ultrahigh Rate and High Capacity for Advanced Lithium-Ion Battery

Jiangtao Hu, Yi Jiang, Suihan Cui, Yandong Duan, Tongchao Liu, Hua Guo, Lingpiao Lin, Yuan Lin, Jiaxin Zheng, Khalil Amine, and Feng Pan*

A 3D-printing technology and printed 3D lithium-ion batteries (3D-printed LIBs) based on $\text{LiMn}_{0.21}\text{Fe}_{0.79}\text{PO}_4$ @C (LMFP) nanocrystal cathodes are developed to achieve both ultrahigh rate and high capacity. Coin cells with 3D-printed cathodes show impressive electrochemical performance: a capacity of $108.45 \text{ mAh g}^{-1}$ at 100 C and a reversible capacity of $150.21 \text{ mAh g}^{-1}$ at 10 C after 1000 cycles. In combination with simulation using a pseudo 2D hidden Markov model and experimental data of 3D-printed and traditional electrodes, for the first time deep insight into how to achieve the ultrahigh rate performance for a cathode with LMFP nanocrystals is obtained. It is estimated that the Li-ion diffusion in LMFP nanocrystal is not the rate-limitation step for the rate to 100 C, however, that the electrolyte diffusion factors, such as solution intrinsic diffusion coefficient, efficiency porosity, and electrode thickness, will dominate ultrahigh rate performance of the cathode. Furthermore, the calculations indicate that the above factors play important roles in the equivalent diffusion coefficient with the electrode beyond a certain thickness, which determines the whole kinetic process in LIBs. This fundamental study should provide helpful guidance for future design of LIBs with superior electrochemical performance.

1. Introduction

Rechargeable lithium-ion batteries (LIBs) play a key role in energy storage devices due to their high power density.^[1] One of the challenges for LIBs is to achieve both a high or ultrahigh charging/discharging rate and high capacity, which is important for portable electronics, electric vehicles, and renewable-energy smart grids. Although super capacitors can charge/discharge

rapidly, their capacities are much lower and the costs are higher compared with LIBs.^[2] Increasing both charge/discharge rates and capacity of LIBs is thus an intensely studied topic.

The rate of electrochemical redox reaction of an electrode depends on the kinetics of the de-intercalation/intercalation of Li^+ ions and loss/gain of electrons at the interface between the electrode and the electrolyte. As a result, the Li intercalation rate inside the bulk materials and the transport of electrons and Li ions to or from the active particles are crucial factors affecting the rate capability. If the Li intercalation rate inside the bulk materials is the rate-limiting step, there are already well-developed methods to improve it. One is to scale particles to nano-size to shorten the Li-ion diffusion path, such as in olivine-based LiMPO_4 ($M = \text{Fe, Mn, Co, or Ni}$).^[3,4] Another is introducing more Ni^{2+} content or enlarging the Li slab space to decrease the diffusion energy barrier in

layered $\text{LiNi}_x\text{Mn}_y\text{Co}_z\text{O}_2$.^[5] And yet another is tuning the temperature to improve the Li-ion diffusion in Li_2MSiO_4 ($M = \text{Fe, Mn, Co, or Ni}$).^[6]

As for the nano-sized particles, the Li intercalation rate inside the nanoparticles is not the limiting step, rather it is the transport of electrons^[7] and Li ions to or from the active nanoparticles.^[3,8–10] Carbon coating is an effective and commonly used method to improve the transport of electrons to the active particles, resulting in significant improvements in rate performance.^[11] If the electric conductivity problem can be solved with a carbon coating, then the next task is to improve the Li transport to and from the active nanoparticles across the solid/liquid interface between nanoparticles and electrolyte, and to increase the Li-ion diffusion in the electrolyte. Kang and Ceder reported that creating a fast ion-conducting surface phase of LiFePO_4 nanocrystals through controlled off-stoichiometry can realize ultrafast charging and discharging.^[12] Yamada et al. reported that a salt-super concentrating rebuilding interface between the electrode and electrolyte realized high voltage and fast charging behavior.^[13] Zheng et al. reported that a “Janus” solid–liquid interface would facilitate the Li-ions spreading across the solid/liquid interface of LiFePO_4 cathodes in aqueous

J. Hu, Y. Jiang, S. Cui, Dr. Y. Duan, T. Liu, H. Guo, L. Lin, Prof. Y. Lin, Prof. J. Zheng, Prof. K. Amine, Prof. F. Pan
School of Advanced Materials
Peking University
Shenzhen Graduate School
Shenzhen 518055, P. R. China
E-mail: panfeng@pku.edu.cn
Prof. K. Amine
Electrochemical Technology Program
Chemical Sciences and Engineering Division
Argonne National Laboratory
Argonne, IL 60439, USA



DOI: 10.1002/aenm.201600856

electrolyte to achieve ultrahigh fast charging–discharging rate of 600 C ($3600/600 = 6$ s charge time, $1\text{ C} = 170\text{ mAh g}^{-1}$) reaching 72 mAh g^{-1} energy storage (42% of the theoretical capacity).^[10] The Li-ion diffusion in the electrolyte could also play a dominant role in the rate performance, when the liquid environment^[10,14] changes or the electrode thickness or the current density is beyond a certain limit.^[9,15,16] For example, dilution of LiFePO_4 active material with TiO_2 can achieve high charging and discharging rates and locally deplete the concentration of Li salt in the electrolyte, which limits further rate improvement.^[17] Based on the above discussion, achieving both ultrahigh rate and high capacity requires coordination of the factors mentioned above, but the related mechanism still needs further exploration.

3D printing technology has rapidly advanced in recent years. This technology can be used to realize rapid prototyping of an object and patterning at low cost^[18] and has been widely used in many areas.^[18,19] Additionally, this method can also control the thickness of electrode as well as the shapes by modifying viscous and speed of the printed material, such as trapezoid, triangle, circular arc, and so on.^[20] Various researchers have employed 3D printing to fabricate LIB electrodes with high performance. Compared with the traditional 2D electrode (planar, getting by coating method), the 3D electrode (getting by 3D printing technology) has the advantages of high areal energy density, short Li-ion transport distance, and increased height of the interdigitated battery.^[21] For example, Sun et al. printed 3D Li-ion microbatteries which exhibited superior areal energy and power densities,^[22] and Delannoy et al. realized high rate charge/discharge behavior of the LiFePO_4 cathode through ink-jet printing.^[23] Moreover, printing technology can control electrode width and thickness by adjusting printing speed and changing the printer nozzle and resulting pressure.

We have developed a 3D-printing technology and printed 3D LIBs based on $\text{LiMn}_{1-x}\text{Fe}_x\text{PO}_4@\text{C}$ nanocrystal cathodes, in which $\text{LiMn}_{1-x}\text{Fe}_x\text{PO}_4$ can take advantage of higher energy density with higher working voltage than that of pure LiFePO_4 because appropriate redox potential of LiMnPO_4 is 4.1 V higher than 3.4 V in LiFePO_4 .^[24] Compared with the traditional coated electrode, such printed 3D LIBs showed ultrahigh rate capability and capacity, demonstrating the highest rate capability among $\text{LiMn}_{0.21}\text{Fe}_{0.79}\text{PO}_4@\text{C}$ (LMFP) cathodes. More important, we employed a pseudo 2D hidden Markov model (P2D-HMM)^[25] and a simplified LIB model simulation to further clarify the relationship between the electrode material layer thickness and the relative rate performance. It is finally found that the electrolyte diffusion on the battery rate performance, such as solution intrinsic diffusion coefficient, efficiency porosity, and electrode thickness, would play a dominant role in determining the whole kinetics process in the LIBs. These results have universal significance and can provide new clues for future battery design to how to achieve both high rate performance and capacity by balancing electrode thickness and optimizing efficiency porosity of electrode.

2. Results and Discussion

Scheme S1 (Supporting Information) presents overviews of the processes used to prepare LIB electrodes by traditional and 3D

printing methods. **Figure 1** describes in detail the 3D printing process designed by us. Our printing equipment contains a movable stage, control system, air-powered dispenser, and the most important part, micronozzle. The main factors affecting the printed electrode morphology are the dispenser pressure, material moving speed, gap between nozzle tip and substrate, and the inner nozzle diameter.^[26] The printing line spacing and width can be adjusted easily. The total printing process is controlled by computer software.

Step I in **Figure 1** shows the synthesis process for the LMFP nanocrystalline electrode material, which involves calcination followed by carbon coating (see details in the Experimental Section). Step II displays the printing process with the resulting slurry, visualized by a magnifying glass, as shown in **Figure 1b**. As shown in **Figure 1c**, the stereo structure of the slurry is built with a 3D confocal microscope, where the printing height and width of the LMFP line are 18 and 450 μm , respectively. The average electrode density of traditional and 3D-electrodes are 534 and 529 kg m^{-3} , which were calculated by dividing volume with quality.

The crystal structure of the material was characterized by X-ray diffraction (XRD) (**Figure S1a**, Supporting Information). The diffraction peaks located at $2\theta = 17.13^\circ$, 20.74° , 25.52° , 29.67° , 35.54° , and 52.43° correspond to the standard diffraction pattern of LMFP (ICSD #54828). The proportions of element Fe and Mn deduced from this figure are very close to measurements with inductively coupled plasma/atomic emission spectroscopy (ICP-AES), and the ratio between them is 3.8 after normalization. At the same time, Rietveld refinement was carried out to estimate the lattice parameters and particle size, as shown in **Figure S1b** (Supporting Information). The particle size of the $\text{LiMn}_{0.21}\text{Fe}_{0.79}\text{PO}_4@\text{C}$ was 44.7 nm. The scanning electron microscopy (SEM) image shows that the $\text{LiMn}_{0.21}\text{Fe}_{0.79}\text{PO}_4@\text{C}$ particles are dispersed very well, and the average particle size is about 40 nm (**Figure S2**, Supporting Information), close to the refinement data. The transmission electron microscopy (TEM) image in **Figure 1a** shows the lattice spacing and carbon coating layer. These lattice fringes have line spacing of 0.35 and 0.39 nm, which match well with the (111) and (021) planes of $\text{LiMn}_{0.21}\text{Fe}_{0.79}\text{PO}_4$. The carbon coating layer is about 1 nm, which plays an important role in protecting the inner active materials and enhancing the electrical conductivity. Thermogravimetric analysis (TGA) of $\text{LiMn}_{0.21}\text{Fe}_{0.79}\text{PO}_4@\text{C}$ and $\text{LiMn}_{0.21}\text{Fe}_{0.79}\text{PO}_4$ (calcined at the same conditions as the former material) under an air atmosphere (**Figure S3a,b**, Supporting Information) shows that the weight percentage of coating carbon layer is about 4.5%, calculated by subtracting the TGA curves for the two electrode materials (**Figure S3c**, Supporting Information).

The charge–discharge curves of 3D-printed and traditional electrodes at 0.5 C are shown in **Figure S4** (Supporting Information). There are two voltage plateaus in the charge and discharge curves, at 4.1 and 3.4 V. These voltages correspond to the redox reaction of iron and manganese, respectively. The cyclic voltammetry (CV) results shown in **Figure S5** (Supporting Information) are in accordance with the two voltage plateaus in charge and discharge.

The rate capabilities of the 3D-printed and traditional electrodes were examined within the voltage window of 2–4.5 V.

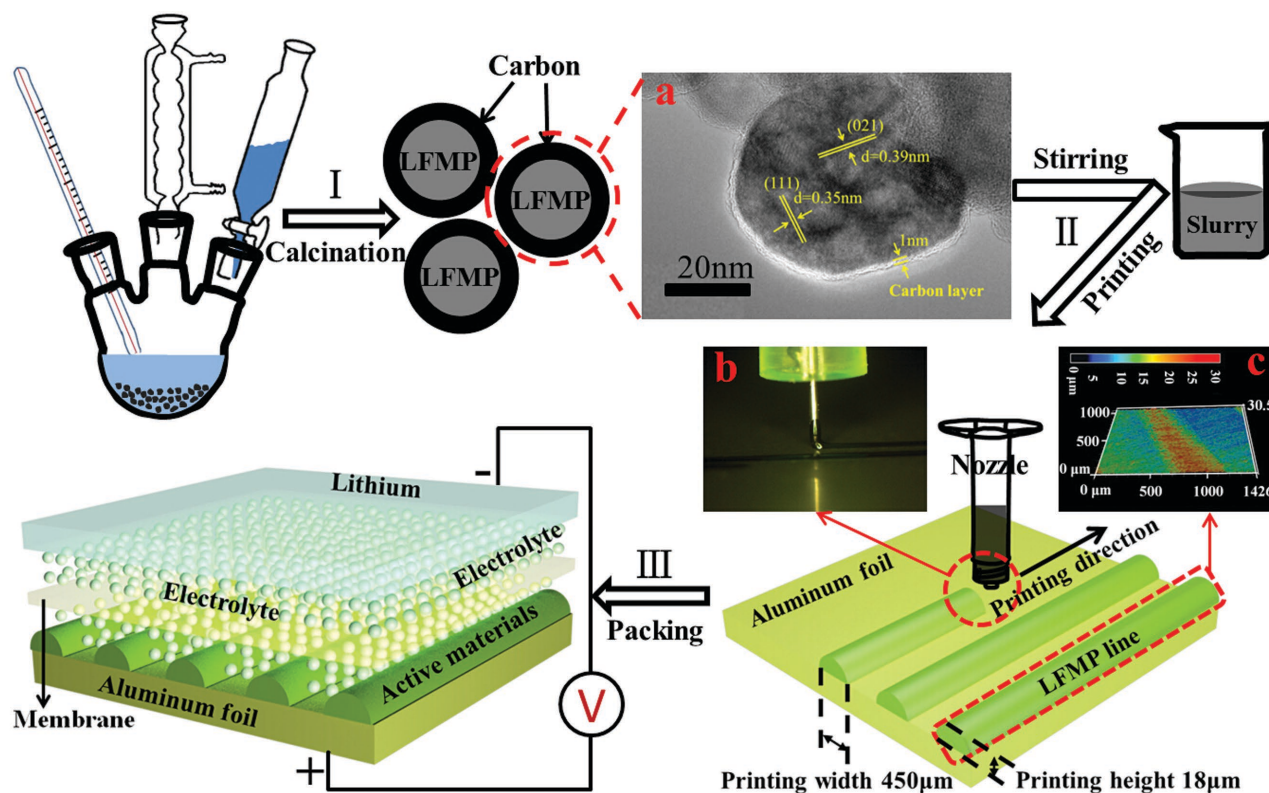


Figure 1. Schematic of battery preparation with the 3D-printed electrode: a) TEM image of $\text{LiMn}_{0.21}\text{Fe}_{0.79}\text{PO}_4\text{@C}$, b) printing process recorded by a magnifying glass, and c) 3D structure of (b) obtained by a 3D confocal microscope (the printing width and height are 450 and 18 μm , respectively).

Figure 2a,b presents the charge–discharge curves of the two electrodes at different rates from 1 C to 100 C. Figure 2c shows that the 3D-printed electrode performed much better than the traditional electrode: the discharge capacity varied much smaller from 161.36 to 108.45 mAh g^{-1} at rates of 1 C to 100 C. In order to verify our rate performance, we reduced the carbon content to 5% and measured the rate performance as shown in Figure S6 (Supporting Information). The specific capacity of 3D-printed electrode at 50 C and 100 C is about 108.8 and 88 mAh g^{-1} . We also collect rate data cycled at different temperature (–20 and 40 $^{\circ}\text{C}$) and full cells data as shown in Figures S7–S9 (Supporting Information). The capacity retention over 1000 cycles for the 3D electrode was also much better, as illustrated in Figure 2d. The capacities of 3D electrode were 150.21 and 140.67 mAh g^{-1} after 1000 cycles at the rates of 10 C and 20 C. By contrast, the corresponding capacities of the traditional electrode were 103.38 and 90.64 mAh g^{-1} . Compared with other olivine materials (Table S2, Supporting Information), the electrochemical performance of this 3D electrode is also the best among them. At the same time, we provide 3D confocal image and the SEM images (the 3D-printed electrode before/after electrochemical test), which verify the stability structure of 3D-printed electrode (Figure S10, Supporting Information). The Electrochemical Impedance Spectroscopy (EIS) data are shown in Figure S11 (Supporting Information), which are in accordance with the electrochemical performance.

To find out why the 3D-printed electrode achieved ultra-high rate performance and capacity, we built a half-cell model,

as shown in Scheme S2 (Supporting Information), and simulated the performance using the P2D model (see details in the Experimental Section). Figure 3a shows the Li-ion concentration in two cells (3D and traditional) under the same charge current, calculated with the P2D model. The only difference between them is the thickness of the porous electrode. It can be seen that the polarization of the Li-ion concentration in the thicker electrode is larger than that in the thinner electrode. As the polarization is caused by the slow Li-ion diffusion, larger polarization indicates lower Li-ion transport in the electrolyte. So Li-ion transport to or from the active materials will rely on Li-ion diffusion in the electrolyte more in the thicker porous electrode than the thinner one under the same conditions.

We further studied the effect of the electrode thickness on the electrochemical behavior of the cells. The volume of the LMFP is about 5/8 of the electrode (LMFP plus XC-72 carbon black plus polyvinylidene fluoride (PVDF) binder, where PVDF accounts for a small volume after drying that can be ignored), and the diameter of the LMFP particles is about 40 nm, so a 36 μm thick electrode is equivalent to about 550 layers of active materials. Scheme S3 (Supporting Information) shows the distribution of the active material layer. We first matched the simulated results for 550 layers with the experimental data of the traditional electrode after normalization. Figure 3b shows the relationship between the number of layers and the simulated capacity (normalized data) at different charging rates (C-rates). It can be seen that our experimental data for the 3D-printed electrode are consistent with the simulation result of 150 layers. It also happens

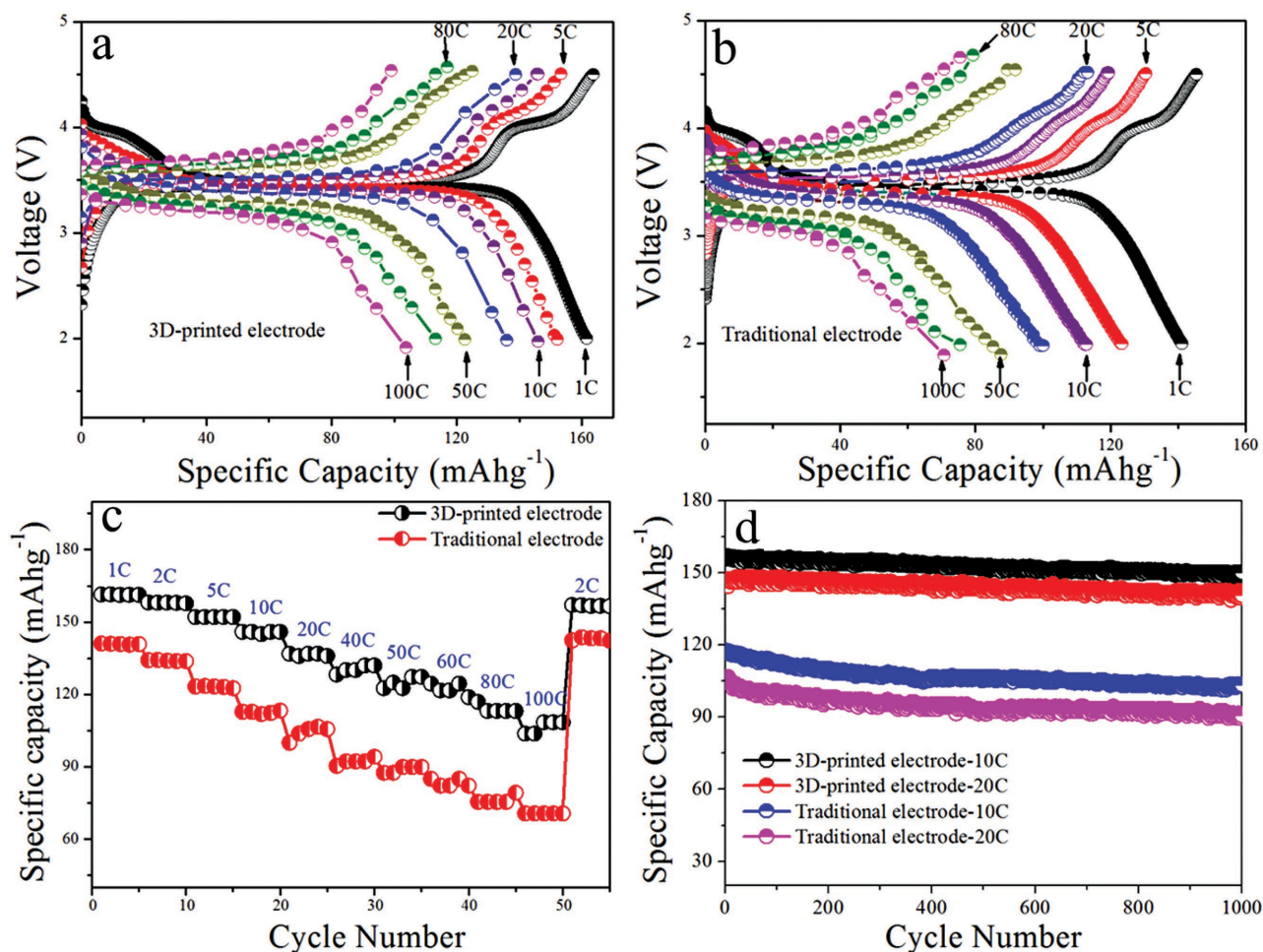


Figure 2. a,b) Charge–discharge voltage curves of 3D-printed and traditional electrodes at different rates (1 C, 5 C, 10 C, 20 C, 50 C, 80 C, and 100 C). c) Rate performance contrast between 3D-printed and traditional electrodes, and (d) capacity of 3D-printed and traditional electrodes at 10 C and 20 C rates for 1000 cycles.

that the equivalent thickness of the 3D-printed electrode is 9 μm , which is just equivalent to about 150 layers (see Equation (S2) in the Supporting Information). When there is only one layer of particles, the capacities of different C-rates are nearly the same (Figure S12, Supporting Information). From 1 C to 100 C, the capacity loss is nearly 0 (less than 0.1 mAh g^{-1}), indicating that nearly all of the Li ions in the active materials have taken part in the chemical reaction, and the capacity is close to the theoretical capacity. As the number of layers increases from 1 to 600, the capacity loss becomes heavier (Figure S13, Supporting Information), indicating that not all the Li ions are intercalated or deintercalated. We attribute the above findings to the rate performance varying under different conditions. We also compared the experimental discharge curves of 3D-printed and traditional electrodes and the simulated discharge curves for 150 and 550 layers (Figure S14, Supporting Information). It can be seen that the two kinds of electrodes exhibit similar discharge curve shapes, and the experimental and calculated curves are in reasonable agreement.

To answer why the 3D-printed electrode has both ultrahigh rate performance and high capacity, the equivalent diffusion

coefficient D_{eq} ($\text{m}^2 \text{ s}^{-1}$, defined in this work, is mainly contributed by solid–liquid interface charge transfer and the liquid diffusion in the article) can provide an explanation. As the bulk diffusion coefficient is several orders of magnitude less than the electrolyte diffusion coefficient, the equivalent diffusion coefficient should be situated between the two. At a certain thickness (550 layers), a parabolic relationship (Figure S15, Supporting Information) is observed between the equivalent diffusion coefficient and the C-rate. By extrapolation from the original calculated equivalent diffusion coefficient of 550 layers at 1 C to 100 C, we can calculate the equivalent diffusion coefficient of different electrode thickness (number of layers) at different C-rates. Calculations showed that, for a given cell, the Li-ion diffusion can be divided into three parts. The inset to Figure 3b shows the determining factor of the overall Li-ion transport at different C-rates and number of layers. On each line parallel to the red line (or the blue line), the equivalent diffusion coefficient is fixed, and the value of the equivalent diffusion coefficient on different lines increases from left to right. The red and the blue lines separate the area into three parts. Zone I (blue region) below the red line corresponds to relatively

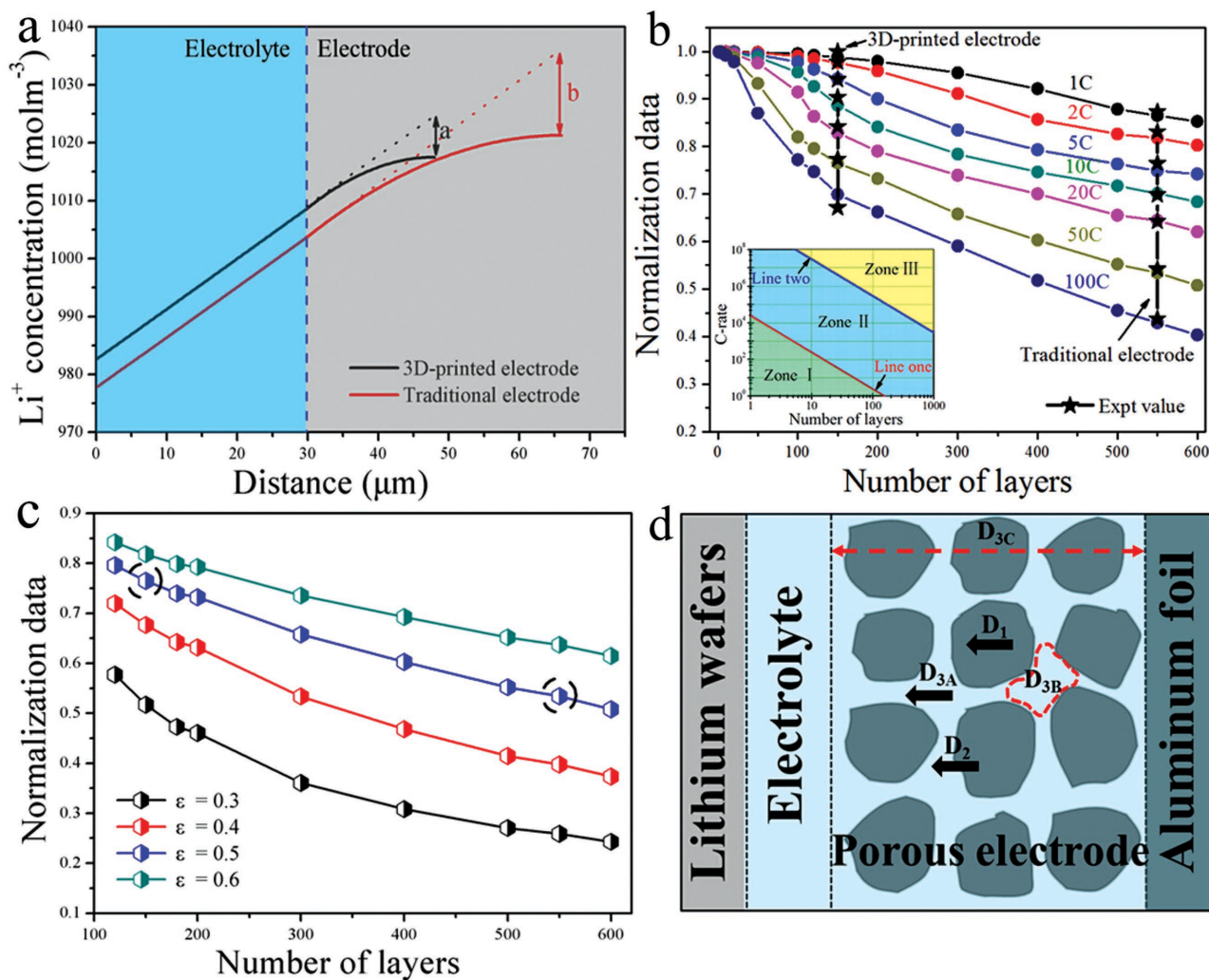


Figure 3. a) Relationship between Li-ion concentration and electrode thickness determined by P2D model. b) Simulation capacity (normalization data) at different C-rates (1 C to 100 C) with different number of layers (the inset illustrates the three types of Li-ion diffusion). c) The simulation capacity with different porosity and number of layers at 50 C rate. d) Factors influencing Li-ion transport: bulk diffusion (D_1), particle interfacial reaction (D_2), solution intrinsic diffusion coefficient (D_{3A}), efficiency porosity (D_{3B}), and electrode thickness (D_{3C}).

smaller C-rates, and the Li-ion diffusion inside the active materials dominates the overall diffusion of the Li ions. In that situation, the Li-ion concentration of the electrolyte in the porous electrode is nearly constant. As a consequence, nearly all the Li-ions in the active materials will take part in the electrochemical reaction, leading to a higher capacity. In Zone I, the thinner the electrode, the higher the C-rate. This is why the 3D-printed electrode works well at a high C-rate while the traditional electrode does not. By contrast, in Zone III (yellow region) above the blue line, the C-rates are the highest, which leads to a larger concentration gradient of the electrolyte in the porous electrode. As the Li ions cannot pass through the porous electrode via bulk diffusion, the electrolyte diffusion and the porosity of electrode would play a dominating role in the overall Li-ion diffusion. In Zone III, the electrochemical reaction at the surface of active materials has to wait for the Li-ion concentration of the electrolyte to reach a more appropriate value. This is why the traditional electrode has less capacity. By contrast, in Zone II,

Li-ion diffusion relies on the combined action between the bulk diffusion and the electrolyte diffusion.

The above model is also consistent with recent reports that in the LiFePO_4 electrodes at high rates, ionic transport through the electrode is rate limiting,^[15] and in electrodes thicker than $\approx 100 \mu\text{m}$, particles closer to the counter electrode lithiate preferentially, reflecting ion transport limitations in the electrolyte.^[9,16] Based on the model above, we can predict that for a cell, given the diameter of the electrode particles, as well as the diffusion coefficients of the bulk and the electrolyte, there must exist boundaries, such as the red and the blue lines inset in Figure 3b, that determine the Li-ion transfer mechanism.

Electrode efficiency porosity also affects Li-ion transport in which the effective diffusion coefficient in the electrolyte is changed due to the change of connectivity within the electrolyte. As Li-ion diffusion inside the active materials dominates the overall diffusion of the Li ions in Zone I, the efficiency porosity mainly dominates in Zones II and III. With

increasing efficiency porosity, the volume fraction of the electrolyte becomes larger, so that the rate of the electrolyte diffusion is increased. For example, the influence of the efficiency porosity on the capacity at the 50 C rate with 120- to 600-layer active material is calculated as shown in Figure 3c, from which the curves show that the capacity of the materials increases with efficiency porosity, and the influence of the efficiency porosity to rate of the electrolyte diffusion becomes larger with increased electrode thickness. Therefore, with the other conditions unchanged, the increasing efficiency porosity would enhance the equivalent diffusion coefficient. Thus, by optimizing efficiency porosity (D_{3B}), the thicker electrode for higher energy density of LIB in the real applications is able to achieve both ultrahigh rate performance and high capacity.

According to the above discussion and previously reported reports,^[17,27] we can summarize the influence of the overall Li-ion diffusion versus rate performance in LIBs. As shown in Figure 3d, the bulk diffusion (D_1), particle interfacial reaction (D_2), and electrolyte diffusion (D_3) are the key factors to overcome the limitations in charge/discharge rates of LIBs. These three factors can be integrated into a simple factor of equivalent diffusion coefficient, which determines the whole kinetics in LIBs. How to balance such factors is very important to realizing high-performance LIBs. There are many reports about how to solve the problems when bulk diffusion (D_1) and particle interfacial reaction (D_2) are the rate-limiting step.^[3,10,13] This work mainly illustrates the influence of electrolyte diffusion (D_3), such as solution intrinsic diffusion coefficient (D_{3A}), efficiency porosity (D_{3B}), and electrode thickness (D_{3C}), as illustrated in Figure 3d.

3. Conclusion

We printed 3D LIBs based on LMFP nanocrystals with 3D printing technology that we developed. The 3D-printed electrode battery delivers 108.45 mAh g⁻¹ at the 100 C rate, ranking it the highest rate capability among LMFP LIBs. It still retains reversible discharge capacities of 150.21 and 140.67 mAh g⁻¹ after 1000 cycles at 10 C and 20 C, respectively, with almost no capacity decay. Through further numerical simulations, we illustrate the influence of electrolyte diffusion (D_3) factors on the battery rate performance, such as solution intrinsic diffusion coefficient (D_{3A}), efficiency porosity (D_{3B}), and electrode thickness (D_{3C}). Such fundamental insight would share important guidance for future design of LIBs with both high capacity and rate capability.

4. Experimental Section

Synthesis of $\text{LiMn}_{0.21}\text{Fe}_{0.79}\text{PO}_4$ @C: $\text{LiMn}_{0.21}\text{Fe}_{0.79}\text{PO}_4$ was synthesized by reflux process and carbonization. Ferrous sulfate/manganous sulfate, phosphoric acid, and lithium hydrate in mole ratio of 1:1.25:2.7 ($\text{FeSO}_4:\text{MnSO}_4 = 8:2$) were dissolved in ethylene glycol. To that end $\text{FeSO}_4/\text{MnSO}_4$ solution was poured into a flask, then the H_3PO_4 and LiOH solutions were successively dropped into the solution slowly under continuous stirring. This mixture was kept for 6 h at 180 °C under the protection of nitrogen. The product was washed with water and ethanol several times, and dried at 70 °C for 6 h in a vacuum. The

resulting product was $\text{LiMn}_{0.21}\text{Fe}_{0.79}\text{PO}_4$, which was coated with carbon. The $\text{LiMn}_{0.21}\text{Fe}_{0.79}\text{PO}_4$ was mixed with 18.5% glucose and 1.5% ascorbic acid, and then the mixture was calcined at 450 °C for 2 h and at 650 °C for 6 h in a quartz tube under the protection of argon. The final product was $\text{LiMn}_{0.21}\text{Fe}_{0.79}\text{PO}_4$ @C.

Structure and Morphology Characterization: The crystallographic structures, morphologies, and ingredients of the final sample were characterized by XRD (Bruker D8 Advance diffractometer using Cu-K α radiation source ($\lambda = 1.54 \text{ \AA}$)), SEM (ZEISS Supra 55), and ICP-AES (JY2000-2). The carbon layer in the $\text{LiMn}_{0.21}\text{Fe}_{0.79}\text{PO}_4$ @C particles is detected by TEM (FEI Tecnai G2 F30). The thermogravimetry-differential scanning calorimetry (TG-DSC) analysis of the $\text{LiMn}_{0.21}\text{Fe}_{0.79}\text{PO}_4$ @C was performed on a TGA/DSC1 system at a heating rate of 10 °C min⁻¹ under airflow. The XPS experiments were performed with an ESCALAB 250XL. The width and height of slurry belt were detected with a 3D confocal microscope (VK-X200 series).

Electrochemical Performance Test: Electrochemical measurements of $\text{LiMn}_{0.21}\text{Fe}_{0.79}\text{PO}_4$ @C electrodes were performed at room temperature with coin cells that had been assembled in an argon-filled glove box. The active materials, XC-72 carbon black, and PVDF were mixed in *N*-methylpyrrolidone under continuous stirring at a proportion of 50:30:20. The obtained slurry was pasted on aluminum foil by 3D printing (the $\text{LiMn}_{0.21}\text{Fe}_{0.79}\text{PO}_4$ @C slurry was carefully transferred to a syringe attached to a micronozzle with 60 μm inner diameter). The slurry was pushed out of the nozzle by pressure coming from a dispenser, where the pressure is 0.45 mPa and the speed of movable material can be as fast as 30 mm s⁻¹ (the gap between nozzle tip and the substrate is controlled around 50 μm). For comparison, electrodes were prepared by the traditional coating method. The two kinds of electrode were named as "3D-printed electrode" and "ordinary or traditional electrode," which were regarded as the working electrode. A Celgard membrane was used as the separator, lithium foil was regarded as the counter electrode and reference electrode, and the electrolyte was 1 M LiPF₆ dissolved in a mixture of ethylene carbonate (EC), diethyl carbonate (DEC), and dimethyl carbonate with a volume ratio of 1:1:1. Electrochemical charge/discharge tests were carried out with a NEWARE battery cycler in a voltage window from 2 to 4.5 V (vs Li⁺/Li) by means of galvanostatic cycling. In order to prove the experimental results, the amount of active material in the electrode was increased to 85% (5% carbon black). Moreover, full battery with graphite and $\text{Li}_4\text{Ti}_5\text{O}_{12}$ (synthesis by ourselves) was assembled. CV measurements were recorded by a CHI electrochemistry workstation (CHI604E series) at a scan rate of 0.5 mV s⁻¹ between 2 and 4.5 V. Electrochemical impedance measurements were performed after different cycle times. All the measurements were carried out at room temperature.

Modeling: The P2D model was used to calculate the relationship between Li-ion concentration of the electrolyte and electrode thickness. The solvent EC:DEC was chosen as the electrolyte. To obtain accurate simulation parameters and results, LiFePO₄ was used as the model electrode material, which has the same structure as $\text{LiMn}_{0.21}\text{Fe}_{0.79}\text{PO}_4$. As a half-cell was tested, the anode (lithium plate) was ignored. The temperature in the half-cell was regarded as constant and was set as 298 K. The flow of the electrolyte was also ignored. In the porous electrode, each active material particle was treated as a sphere. Besides, the volume change of LFP particles during lithiation and delithiation was not taken into consideration. The volume change of LiFePO₄ during lithiation and delithiation was about 6.81%,^[28] and the LFP particles coated with carbon were embedded with conductive carbon black (about 30%) with close contact in the electrode. Thus, it can be expected that the change of electrode structure and particle-to-particle contact resistance will be small during lithiation and delithiation.

As the Li-ion transport in the cell is influenced by many factors, such as bulk diffusion, electrolyte diffusion, electrode porosity, and so on, these factors were synthesized into one factor, called the "equivalent diffusion coefficient" (D_{eq} , m² s⁻¹). Because porosity can influence electrolyte diffusion at a relatively high C-rate, it can be treated as a sub-factor of the electrolyte diffusion. So a new simplified model was developed.

It was assumed that the porous electrode is composed of several layers of particles, which are close packed, and the electrochemical reaction only takes place at the interface of the electrolyte and the electrode. As a result, in the electrode, the equivalent diffusion was only taken into account. The porosity has been considered in the electrolyte diffusion. Besides, to the best of our knowledge, an accurate reaction coefficient has never been reported. So the reaction coefficient was set as a constant and it was assumed the reaction is not the rate-determining step, though it truly influences the Li-ion transport.

In this way, the Butler–Volmer equation only works at the interface between the porous electrode and the electrolyte

$$i_v = i_0 (C_R \exp((1-\alpha)f\eta) - C_o \exp(-\alpha f\eta)) \quad (1)$$

where i_0 ($A\ m^{-2}$) is the density of exchange current, α is the transfer coefficient, $f = F/RT = 38.9\ V^{-1}$ (F is Faraday constant, R is gas constant, and T is temperature), η (V) is the overpotential, C_R (1) and C_o (1) are the concentration ratio of the reductant and the oxide, respectively. i_v ($A\ m^{-2}$) was calculated, which is the current density on the interface of the electrode and electrolyte. For Li-ion diffusion in the electrode, Fick's law can be used directly, as shown below along with the boundary and the initial conditions

$$\frac{\partial C_s}{\partial t} = D_{eq} \frac{\partial^2 C_s}{\partial x^2} \quad (2)$$

$$\frac{\partial C_s}{\partial x} = 0 (x=0)$$

$$\frac{\partial C_s}{\partial x} = i_v / F D_{eq} (x=L_e)$$

$$C_s(x, t=0) = C_{s0} (0 \leq x \leq L_e)$$

where C_s ($mol\ m^{-3}$) is the Li-ion concentration in the solid electrode ($LiFePO_4$), L_e (m) is the electrode thickness, and C_{s0} ($mol\ m^{-3}$) is the initial Li-ion concentration of $LiFePO_4$. The diffusion equation for the electrolyte is similar to that of the electrode

$$\frac{\partial C_l}{\partial t} = D_l \frac{\partial^2 C_l}{\partial x^2} \quad (3)$$

$$\frac{\partial C_l}{\partial x} = -i_v / F D_{eq} (x=L_e)$$

$$\frac{\partial C_l}{\partial x} = 0 (x=L_e + L_l)$$

$$C_l(x, t=0) = C_{l0} (0 \leq x \leq L_e + L_l)$$

where C_l ($mol\ m^{-3}$) is the Li-ion concentration in the electrolyte, L_l (m) is the electrolyte thickness, C_{l0} ($mol\ m^{-3}$) is the initial Li-ion concentration for the electrolyte, and D_l ($m^2\ s^{-1}$) is the Li-ion diffusion coefficient of the electrolyte.

When the number of layers becomes large, for convenience, the reaction was still considered to take place at the interface, and the electrolyte in the porous electrode to only help the Li-ion transport. The values and the physical significance of the parameters are shown in Table S1 (Supporting Information).

Some assumptions about the porosity were also made. According to Bruggeman's effective medium approach, the volume fraction should be taken into account, and higher volume fraction means larger effective diffusion coefficient

$$D_{l,eff} = D_l \varepsilon^{1.5} \quad (4)$$

where ε is the volume fraction and $D_{l,eff}$ ($m^2\ s^{-1}$) is the effective electrolyte diffusion coefficient. For simplicity, it is supposed that the porous electrode is composed of the active materials ($LiFePO_4$) due to about 80% in LMFP and the electrolyte. Therefore, the volume fraction of the electrolyte is equal to the porosity. Another assumption is that the porosity is set between 0.3 and 0.6. When the porosity is low, the electrolyte in the porous electrode may be disconnected, which may cause some parts of the electrolyte surrounded by the active materials and difficult to take part into the reaction. Oppositely, high porosity may lead to the active materials particles distract in the electrolyte, which may cause some of the active materials particles hard to get or lose electrons and disabled to contribute their entire capacity. In this paper, the volume of the LMFP and the carbon with their mass divided by their density, respectively, was calculated. Here the solid volume fraction ε_s (the ratio of the volume of LMFP and carbon to the total volume of the porous electrode) is 0.40–0.55. Thus, the porosity is approximate to $1 - \varepsilon_s$, with the value of 0.45–0.60. As the thickness is not uniform, the estimation of the total volume may be not so accurate. Besides, the volume of PVDF is ignored, so the true porosity may be a little less than the estimated value. Through the estimation, a range of the porosity can only be obtained. But to study the influence of the thickness, it is assumed that the porosity is a constant and it was set to 0.5.

Supporting Information

Supporting Information is available from the Wiley Online Library or from the author.

Acknowledgements

J.H., Y.J., and S.C. contributed equally to this work. The authors thank Argonne National Laboratory for the enthusiastic help of this work. The research was financially supported by National Project for EV Batteries (20121110, Optimum Nano, Shenzhen), Guangdong Innovation Team Project (No. 2013N080), and Shenzhen Science and Technology Research Grant (No. ZDSY20130331145131323).

Received: April 24, 2016

Published online:

- [1] a) M. Armand, J. M. Tarascon, *Nature* **2008**, *451*, 652; b) A. Yoshino, *Angew. Chem. Int. Ed. Engl.* **2012**, *51*, 5798; c) F. Cheng, J. Liang, Z. Tao, J. Chen, *Adv. Mater.* **2011**, *23*, 1695.
- [2] Z. Yang, J. Zhang, M. C. W. Kintner-Meyer, X. Lu, D. Choi, J. P. Lemmon, J. Liu, *Chem. Rev.* **2011**, *111*, 3577.
- [3] R. Malik, A. Abdellahi, G. Ceder, *J. Electrochem. Soc.* **2013**, *160*, A3179.
- [4] K. Zaghbi, A. Guerfi, P. Hovington, A. Vijh, M. Trudeau, A. Mauger, J. B. Goodenough, C. M. Julien, *J. Power Sources* **2013**, *232*, 357.
- [5] Y. Wei, J. Zheng, S. Cui, X. Song, Y. Su, W. Deng, Z. Wu, X. Wang, W. Wang, M. Rao, Y. Lin, C. Wang, K. Amine, F. Pan, *J. Am. Chem. Soc.* **2015**, *137*, 8364.
- [6] R. Tan, J. Yang, J. Zheng, K. Wang, L. Lin, S. Ji, J. Liu, F. Pan, *Nano Energy* **2015**, *16*, 112.
- [7] Y. Li, S. Meyer, J. Lim, S. C. Lee, W. E. Gent, S. Marchesini, H. Krishnan, T. Tyliczszak, D. Shapiro, A. L. D. Kilcoyne, W. C. Chueh, *Adv. Mater.* **2015**, *27*, 6590.
- [8] M. Valtiner, S. Borodin, G. Grundmeier, *Phys. Chem. Chem. Phys.* **2007**, *9*, 2406.
- [9] J. Liu, M. Kunz, K. Chen, N. Tamura, T. J. Richardson, *J. Phys. Chem. Lett.* **2010**, *1*, 2120.

- [10] J. Zheng, Y. Hou, Y. Duan, X. Song, Y. Wei, T. Liu, J. Hu, H. Guo, Z. Zhuo, L. Liu, Z. Chang, X. Wang, D. Zherebetsky, Y. Fang, Y. Lin, K. Xu, L. W. Wang, Y. Wu, F. Pan, *Nano Lett.* **2015**, *15*, 6102.
- [11] a) J. Wang, J. Yang, Y. Zhang, Y. Li, Y. Tang, M. N. Banis, X. Li, G. Liang, R. Li, X. Sun, *Adv. Funct. Mater.* **2013**, *23*, 806; b) J. Wang, X. Sun, *Energy Environ. Sci.* **2012**, *5*, 5163; c) N. Ravet, Y. Chouinard, J. F. Magnan, S. Besner, M. Gauthier, M. Armand, *J. Power Sources* **2001**, *97–8*, 503.
- [12] B. Kang, G. Ceder, *Nature* **2009**, *458*, 190.
- [13] Y. Yamada, K. Usui, C. H. Chiang, K. Kikuchi, K. Furukawa, A. Yamada, *ACS Appl. Mater. Interfaces* **2014**, *6*, 10892.
- [14] Q. Wang, S. M. Zakeeruddin, I. Exnar, M. Gratzel, *J. Electrochem. Soc.* **2004**, *151*, A1598.
- [15] X. Zhang, T. W. Verhallen, F. Labohm, M. Wagemaker, *Adv. Energy Mater.* **2015**, *5*, 1500498.
- [16] a) D. Robert, T. Douillard, A. Boulineau, G. Brunetti, P. Nowakowski, D. Venet, P. Bayle-Guillemaud, C. Cayron, *ACS Nano* **2013**, *7*, 10887; b) F. C. Strobridge, B. Orvananos, M. Croft, H.-C. Yu, R. Robert, H. Liu, Z. Zhong, T. Connolley, M. Drakopoulos, K. Thornton, C. P. Grey, *Chem. Mater.* **2015**, *27*, 2374.
- [17] P. A. Johns, M. R. Roberts, Y. Wakizaka, J. H. Sanders, J. R. Owen, *Electrochem. Commun.* **2009**, *11*, 2089.
- [18] B. C. Gross, J. L. Erkal, S. Y. Lockwood, C. Chen, D. M. Spence, *Anal. Chem.* **2014**, *86*, 3240.
- [19] a) W. Wu, A. DeConinck, J. A. Lewis, *Adv. Mater.* **2011**, *23*, H178; b) C. Liu, Z. Xia, J. T. Czernuszka, *Chem. Eng. Res. Design.* **2007**, *85*, 1051.
- [20] C. Ladd, J. H. So, J. Muth, M. D. Dickey, *Adv. Mater.* **2013**, *25*, 5081.
- [21] a) S. Ferrari, M. Loveridge, S. D. Beattie, M. Jahn, R. J. Dashwood, R. Bhagat, *J. Power Sources* **2015**, *286*, 25; b) J. W. Long, B. Dunn, D. R. Rolison, H. S. White, *Chem. Rev.* **2004**, *104*, 4463.
- [22] K. Sun, T. S. Wei, B. Y. Ahn, J. Y. Seo, S. J. Dillon, J. A. Lewis, *Adv. Mater.* **2013**, *25*, 4539.
- [23] P. E. Delannoy, B. Riou, T. Brousse, J. Le Bideau, D. Guyomard, B. Lestriez, *J. Power Sources* **2015**, *287*, 261.
- [24] a) H. Wang, Y. Yang, Y. Liang, L.-F. Cui, H. S. Casalongue, Y. Li, G. Hong, Y. Cui, H. Dai, *Angew. Chem.* **2011**, *123*, 7502; b) A. Paoella, G. Bertoni, E. Dilena, S. Marras, A. Ansaldo, L. Manna, C. George, *Nano Lett.* **2014**, *14*, 1477; c) D. D. Lecce, J. Hassoun, *J. Phys. Chem. C* **2015**, *119*, 20855.
- [25] a) M. Doyle, T. F. Fuller, J. S. Newman, *J. Electrochem. Soc.* **1993**, *140*, 1526; b) V. Ramadesigan, P. W. C. Northrop, S. De, S. Santhanagopalan, R. D. Braatz, V. R. Subramanian, *J. Electrochem. Soc.* **2012**, *159*, R31.
- [26] X. Chen, K. Church, H. Yang, I. B. Cooper, A. Rohatgi, *Photovoltaic Specialists Conference (PVSC)*, IEEE, Seattle, WA, **2011**, 3667.
- [27] a) A. A. Franco, *RSC Adv.* **2013**, *3*, 13027; b) P. M. Biesheuvel, Y. Fu, M. Z. Bazant, *Phys. Rev. E* **2011**, *83*, 061507; c) P. M. Biesheuvel, M. Z. Bazant, *Phys. Rev. E* **2010**, *81*, 031502; d) M. Gaberscek, M. Kuzma, J. Jamnik, *Phys. Chem. Chem. Phys.* **2007**, *9*, 1815; e) R. Zhao, M. van Soestbergen, H. H. Rijnaarts, A. van der Wal, M. Z. Bazant, P. M. Biesheuvel, *J. Colloid Interface Sci.* **2012**, *384*, 38; f) L. Ke, W. Lv, F.-Y. Su, Y.-B. He, C.-H. You, B. Li, Z. Li, Q.-H. Yang, F. Kang, *Carbon* **2015**, *92*, 311.
- [28] A. K. padhi, K. S. Nanjundaswamy, J. B. Goodenough, *J. Electrochem. Soc.* **1997**, *144*, 1188.